# Growth of Ultrahigh Density Single-Walled Carbon Nanotube Forests by Improved Catalyst Design

**Guofang Zhong,[†] Jamie H. Warner,[‡] Martin Fouquet,[†] Alex W. Robertson,[‡] Bingan Chen,[†] and John Robertson[†,*]**

[†]Department of Engineering, University of Cambridge, Cambridge CB3 0FA, United Kingdom and [‡]Department of Materials, University of Oxford, Oxford OX1 3PH, United Kingdom

**ABSTRACT**

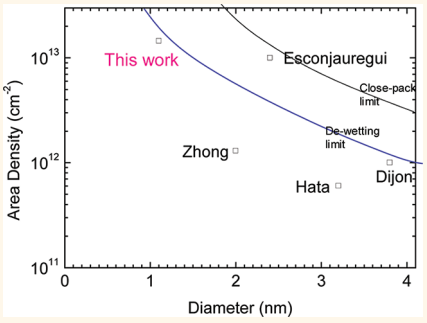


**We have grown vertically aligned single-walled carbon nanotube forests with an area density of 1.5 × $10^{13}$ cm$^{-2}$, the highest yet achieved, by reducing the average diameter of the nanotubes. We use a nanolaminate Fe—$Al_2O_3$ catalyst design consisting of three layers of $Al_2O_3$, Fe, and $Al_2O_3$, in which the lower $Al_2O_3$ layer is densified by an oxygen plasma treatment to increase its diffusion barrier properties, to allow a thinner catalyst layer to be used. This high nanotube density is desirable for using carbon nanotubes as interconnects in integrated circuits.**

**KEYWORDS:** single-walled carbon nanotubes · vertical forest · chemical vapor deposition · ultrahigh density · characterization · catalyst preparation

Single-walled carbon nanotubes (SWNTs) have many potential applications in areas such as electronics, energy storage, stiff composites, and sensors due to their unique properties.[1−3] This has led to considerable efforts to improve the carbon nanotube growth process using the catalytic chemical vapor deposition (CVD) method, whether for nanotubes grown as vertically aligned forests on surfaces[4−7] or grown in bulk reactors. For nanotube forests, there has been extensive work to maximize the growth rates and the catalyst lifetimes.[8−18]

In electronics, carbon nanotubes (CNTs) have great potential to replace copper as interconnects in integrated circuits because they are the only material capable of carrying high current densities over $10^8$ A/cm$^2$.[19−31] This application is more important to the semiconductor roadmap than, for example, the use of SWNTs as semiconductors in field-effect transistors.[19] However, CNTs will not be used as interconnects unless the interconnect resistance is as low as that of the copper that it replaces. Each wall of a CNT is a one-dimensional conductor, and this will introduce a series resistances from their quantum of conductance. To reduce this resistance, we must parallel many CNTs, and this requires CNTs to be grown in densities of at least 2 × $10^{13}$ cm$^{-2}$.[20]

The densest standard forests grown to date by Futaba *et al.*[1] or Zhong *et al.*[10] use Fe as catalyst and $Al_2O_3$ as support layer. They have an area density of 7 × $10^{11}$−$10^{12}$ cm$^{-2}$. This is high, but it is still a factor of ∼30 too low for the interconnect applications. On the other hand, typical forests grown specifically as interconnects, until recently, had densities only in the $10^{10}$ cm$^{-2}$ range.[22,23] The low densities are a key reason that CNT interconnects have not yet been implemented by electronics manufacturers. There is therefore an urgent drive to increase the CNT forest area density. Most of the effort in nanotube forest growth is directed toward maximizing yield, by increasing the growth rate or catalyst lifetime.[7−17] In contrast, interconnects require a focus on quality—area density.

Figure 1 shows a close-packed array of cylinders of diameter, $D$, representing nanotubes and separated by a distance $\delta$. It turns out that existing forests are not particularly dense, occupying only about 5% of the available area, as $D \ll \delta$. Thus, there are two ways to increase nanotube density, either increase the packing fraction by reducing $\delta$ or reduce the nanotube diameter, assuming that $\delta$ scales with $D$.

* Address correspodence to jr@eng.cam.ac.uk.

Received for review May 31, 2011 and accepted March 22, 2012.

**Published online March 23, 2012**
**10.1021/nn203035x**

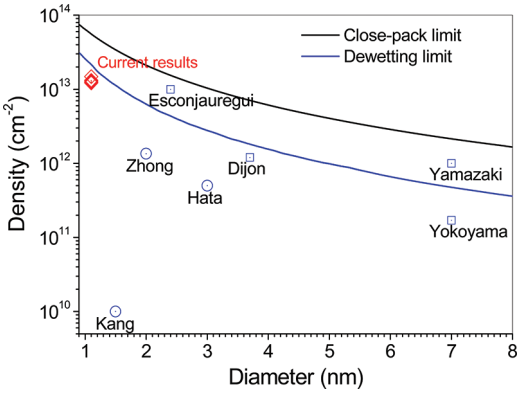


**Figure 1. Area density *vs* average nanotube diameter for carbon nanotube forests, compared to that expected from the dewetting mechanism and the ideal close-packed limit. Also shown are data from previous groups,[1,10,23,25,28] including data for horizontally grown nanotubes.[43]**

The diameter of SWNTs prepared by many methods is about 1.0−1.2 nm, whether grown by laser ablation, HiPCO, or CVD using the CoMoCAT catalyst.[32−36] A similar diameter is found using ferritin as catalyst,[33] which is a well-defined nanocluster of Fe in an organic shell. On the other hand, forest growth uses the Fe/$Al_2O_3$ catalyst/support combination because this presently maximizes the catalyst efficiency and yield,[6−12] but it tends to give CNTs with a larger than average diameter, typically in the 2.0−4.0 nm range. This means that the area density of these forests is not as high as possible.

The present paper describes a catalyst design that greatly increases the nanotube area density by a factor of 20-fold over previous densities, by reducing the nanotube diameter.

**Catalyst Modeling.** We first analyze the factors that control the nanotube area density. In CVD, ideally one nanotube grows from each catalyst nanoparticle, so that the density and diameter of the nanotubes are the same as those of the original catalyst nanoparticles. The catalyst is usually deposited as a thin film and then annealed. This converts the catalyst film into a series of nanoparticles by a dewetting process that is driven by the difference in surface energy of the catalyst and the underlying support layer.[37]

The interfacial energy of an ideal thin film of thickness $h$ on a substrate is given by $G_1 = A(\sigma_1 + \sigma_{12})$, where $\sigma_1$ is the catalyst surface energy, $\sigma_{12}$ is the catalyst−support interface energy, and $A$ is the support area per nanoparticle. The interfacial energy of a truncated spherical ball of top surface area $S_2$ in contact with the flat surface is given by $G_2 = (A - S_{12})\sigma_2 + S_2\sigma_1 + S_{12}\sigma_{12}$, where $\sigma_2$ is the support surface energy and $S_{12}$ is the contact area. The contact angle $\theta$ of the truncated sphere is given by Young's equation $\sigma 2 = \sigma_{12} + \sigma_1 \cos(\theta)$.

The minimum diameter of the nanoparticles formed by dewetting occurs when $G_2 = G_1$. Using conservation of catalyst volume, the nanoparticle diameter $D$ will vary with initial film thickness $h$ as

$$D = \frac{6h \sin\theta}{1 - \cos\theta} \quad \textbf{(1a)}$$

or

$$D = \frac{6h}{1 - \cos\theta} \quad \textbf{(1b)}$$

if $\theta > 90°$. This results in a nanoparticle density $N$ of

$$N = \frac{4}{\pi D^2}\frac{(1 + \cos\theta)}{(2 + \cos\theta)} \quad \textbf{(2a)}$$

or

$$N = \frac{4}{\pi D^2(1 - \cos\theta)(2 + \cos\theta)} \quad \textbf{(2b)}$$

if $\theta > 90°$. On the other hand, the maximum theoretical density of straight, uniform, vertically aligned nanotubes of diameter $D$ occur if they form a hexagonal array separated by the $c$-axis spacing of graphite, $\delta$ = 0.34 nm

$$N = \frac{2}{\sqrt{3}(D+\delta)^2} \quad \textbf{(3)}$$

Figure 1 plots this maximum density and the density for the dewetting mechanism as a function of $D$ for $\theta \sim 90°$, a typical contact angle seen in *in situ* TEM[38] and compares it to the nanotube densities in some forests of previous groups. We see that the densest forests lie around the dewetting limit. It is clear that to increase the nanotube density above existing values, from eq 2, we must either decrease the diameter $D$ or increase the density beyond the dewetting limit.

A typical initial catalyst thickness $h$ is 1 nm. This would give nanotubes of diameter $D \sim 6h = 4-6$ nm.[1] This is quite large compared to the 1.0 nm diameter CNTs grown by the HiPCO or laser methods.[32,33] Clearly, from eqs 1 and 2, the simplest way to increase density is to decrease the catalyst film thickness. However, as $h$ is decreased, nucleation becomes less reliable and the nanotube yield decreases, due to various factors such as the diffusion of the catalyst into the support layer. A typical example is that of Noda *et al.*,[7,39] who found a decline in yield for Fe thickness below 0.5 nm.

The densest forests are generally grown using the Fe:$Al_2O_3$ catalyst:support system.[1,4,6−16,39] $Al_2O_3$ works because it inhibits the surface diffusion and sintering of the Fe nanoparticles, helped by an interfacial reaction of the Fe on $Al_2O_3$.[40] However, $AlO_x$ can be porous, and it may not inhibit Fe diffusion away from the surface. $AlO_x$ formed in different ways is known to behave differently as a catalyst support[41] because its surface area and diffusion properties can vary. $AlO_x$ can be deposited as $Al_2O_3$ by evaporation, sputtering or atomic layer deposition (ALD), or deposited as Al metal and

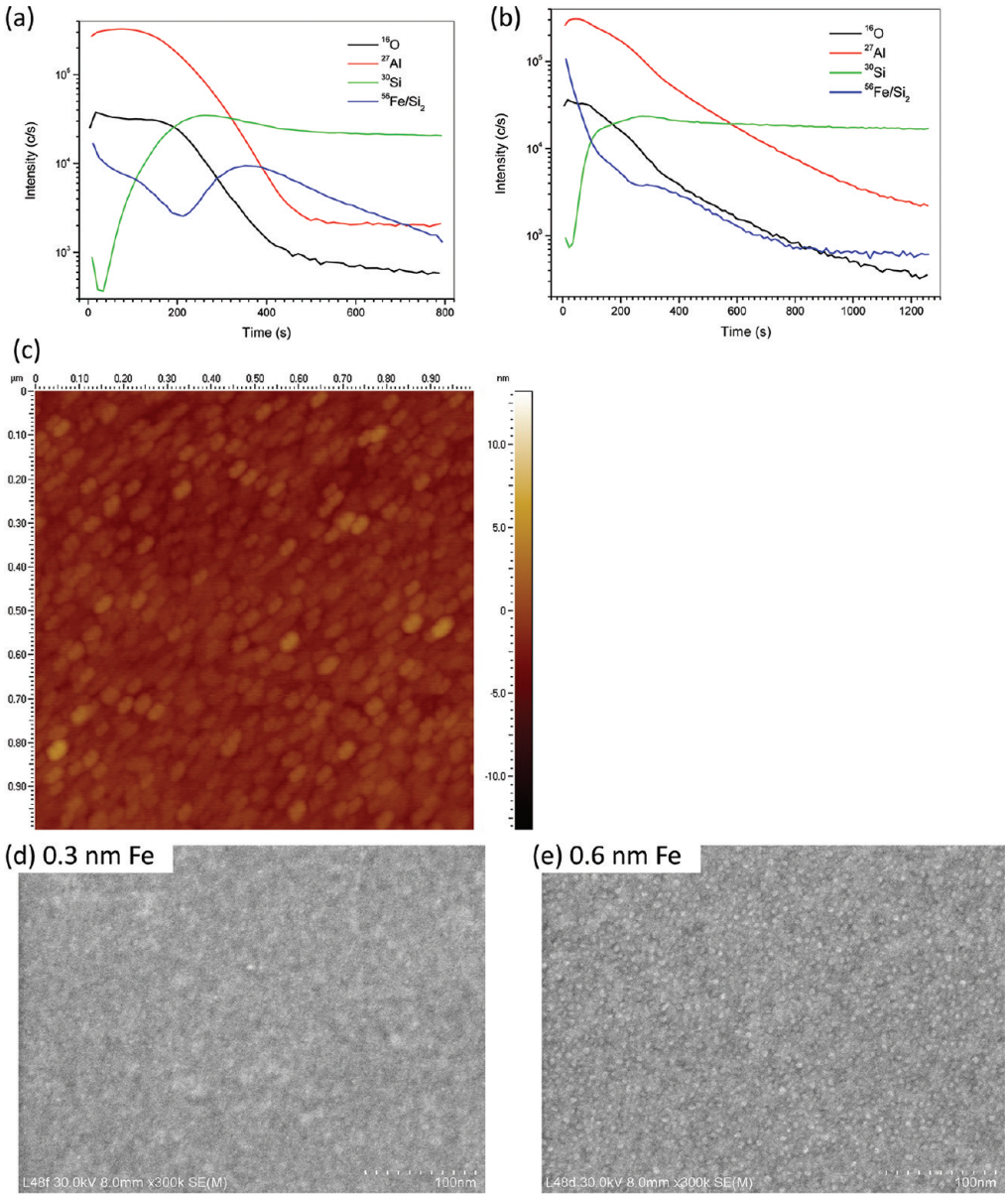


**Figure 2. SIMS depth profiles of a sandwich catalyst nanostructure of 0.5 nm Al (top layer)/0.6 nm Fe/5 nm Al sputtered coated on Si(100), (a) without and (b) with plasma oxidation treatment. (c) AFM image of the support layer after $O_2$ plasma treatment. (d,e) SEM images of Fe on $Al_2O_3$ for 0.3 nm thick Fe and 0.6 nm thick Fe, showing the decrease in particle size for the 0.3 nm case.**

oxidized to $AlO_x$ by ambient or residual oxygen. Here, we used a three-layer catalyst−support design, in which a 5 nm Al layer is sputtered, followed by a 0.7 nm Fe layer, and finally a thin 0.5 nm Al capping layer was sputtered. Previously, we allowed Al to be oxidized to $AlO_x$ by exposure to air. The function of the top (discontinuous) 0.5 nm $AlO_x$ layer is to inhibit surface Fe diffusion, without covering the Fe.

## RESULTS AND DISCUSSION

To check inward diffusion, we have analyzed the elemental depth profiles in the Fe:$Al_2O_3$ layers after a thermal anneal cycle (see Methods) but prior to growth by secondary ion mass spectrometry (SIMS) spectroscopy. Fe, Al, and O were detected by SIMS throughout the layers (Figure 2a). The Fe concentration (blue) decreases monotonically with depth until the $AlO_x$/Si interface, where a peak appears. The peak arises from an accumulation of Fe that diffused into the $AlO_x$ and was then blocked at the Si interface. If nanotubes cannot grow once covered by an $AlO_x$ layer ~1.5 nm thick, then Figure 2 shows that almost half of the Fe catalyst is subsurface and is effectively lost to growth activity. This is a reason that may have limited CNT densities to $10^{12}$ $cm^{-2}$.

In order to increase catalyst effectiveness, we prepared a more diffusion-resistant support layer. We sputtered a 5 nm Al layer and subjected this to a room

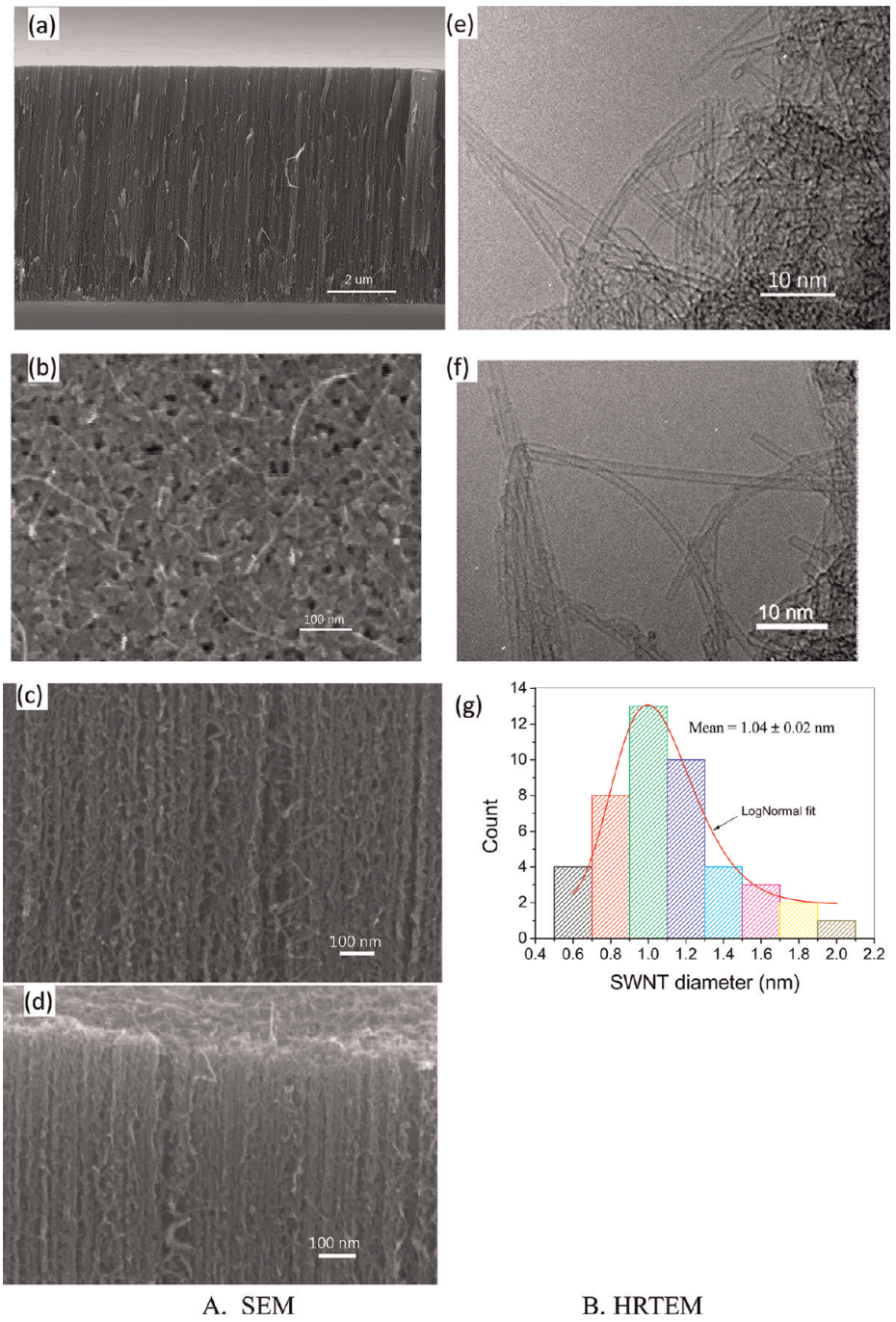


**Figure 3. SEM (A) and HRTEM (B) images of ultrahigh density SWNT forests prepared on 0.5 nm Al/0.4 nm Fe/5 nm Al/Si(100) at 15 mbar, 700 °C, 40 sccm $C_2H_2$ and 460 sccm $H_2$ by cold-wall CVD. The 5 nm Al layer had an $O_2$ plasma treatment. (a) Tilt view of the as-grown sample. (b–d) Surface, side, and tilt views at higher magnifications. (e,f) High magnification HRTEM images of the SWNTs. (g) SWNT diameter distribution from HRTEM images.**

temperature $O_2$ plasma treatment. This was followed by deposition of a 0.3, 0.4, or 0.7 nm Fe catalyst layer, followed by a 0.5 nm top Al layer. The $O_2$ plasma creates a denser, fully oxidized under-layer of $Al_2O_3$. Figure 2b shows the SIM profile for the case of plasma oxidation treatment, again after the thermal annealing of the catalyst/support layers. The Fe concentration (blue) now declines monotonically with no subsurface peak. The surface Fe concentration is also higher. The $Al_2O_3$ layer could also be made by ALD and then plasma oxidized to ensure full densification.

This more impermeable $Al_2O_3$ layer allows us to use a thinner Fe catalyst layer, which, by eq 2, leads to a lower CNT diameter and a higher density. Figure 2c shows an AFM image of the first $Al_2O_3$ layer after the $O_2$ plasma treatment. Figure 2d,e compares SEM images of the Fe catalyst nanoparticles after annealing for Fe films of an initial thickness of 0.3 and 0.6 nm. The 0.3 nm

thick Fe case is seen to have much smaller diameter particles.

A second factor to increase the CNT density is to use a higher $C_2H_2$ concentration. Previously, we used a remote methane plasma[6] in which the plasma created $C_2H_2$ *in situ*, the active growth species. The same growth was then reproduced in a cold wall, purely thermal CVD system at 700 °C,[42] using $H_2$ diluted $C_2H_2$ at a total pressure of 15 mbar. Here, we increased the $C_2H_2$ gas flow ratio to 8%. The higher $C_2H_2$ concentration may promote nucleation and growth of denser forests. A third factor is our use of a cold wall CVD chamber which allows rapid sample heating in a pure $H_2$ flow for about 5 min. This rapid heating may suppress catalyst Ostwald ripening and subsurface diffusion.

Figure 3a−f shows the characterization of the resulting nanotube forests by SEM and high-resolution transmission electron microscopy (HRTEM). Their most significant features include the following. (1) The forests have the highest *area* density seen so far for direct growth, as seen in the higher magnification SEM images in Figure 3c,d. (2) The upper surface of the forest is very smooth. They have fewer surface cracks, often seen in previous SWNT forests, due to van der Waals attraction between adjacent nanotubes.[6] (3) The mean nanotube diameter is much smaller and its distribution is narrower than our previous SWNT forests[11] (Figure 3e−g). (4) The forests are shorter than previously, only several micrometers high (Figure 3a), as growth terminates in a few minutes. The higher density may cause diffusion-limited gas access.[11,18] Nevertheless, the SWNT height is enough for interconnect applications. The HRTEM images in Figure 3e,f show that the forest consists of high-quality SWNTs with little amorphous carbon on their side walls. The average diameter is 1.0 nm, and the diameter follows a log-normal distribution. The diameter does not vary with height in the forest. The diameter distribution of 0.5−2.1 nm is narrower than our previous range of 0.5−4 nm.[11] This is the key result, which allows the higher density to be achieved by the thinner catalyst layer.

There are three basic methods which could be used to measure the nanotube area density: first by counting tubes in the TEM images, second by measuring the sample weight gain during growth, the mean diameter and number of walls from TEM, and thereby deriving the weight per unit length of a nanotube, and thus the area density, and finally using the liquid-induced compaction method and average diameter to find the space filling factor and thus the area density. Counting is less reliable and was not used quantitatively. The liquid compaction method is useful for speed, guidance, and it indicates the uniformity with height. It can also be used in patterned structures.[28] Weight gain is the most quantitative method, and it is used here wherever possible, but it requires relatively high forests. Our data generally come from this method. All three methods give consistent results.[28]

**TABLE 1. Properties of Six Forest Samples Grown at 8% $C_2H_2$ 15 mbar Total Pressure and 700 °C on 0.5 nm Al/0.3 nm Fe/5 nm Al/Si(100)[a]**

| sample | 1 | 2 | 3 | 4 | 5 | 6 |
|---|---|---|---|---|---|---|
| catalyst thickness (nm) | 0.3 | 0.3 | 0.4 | 0.3 | 0.3 | 0.3 |
| mass gain (mg) ±0.003 mg | 0.26 | 0.26 | 0.20 | 0.35 | 0.27 | 0.32 |
| forest height ($\mu$m) | 9.9 | 7.9 | 6.0 | 9.5 | 8.9 | 8.3 |
| mass density (g/cm$^3$) ±0.004 | 0.248 | 0.298 | 0.345 | 0.365 | 0.298 | 0.382 |
| area density ($10^{13}$ cm$^{-2}$) ±0.02 | 1.07 | 1.28 | 1.48 | 1.57 | 1.28 | 1.64 |

[a] The initial catalyst film thickness, mass gain during growth, forest growth height, the resulting mass density and area density are tabulated.

Table 1 summarizes the weight gain method data for three samples. The initial Fe catalyst thickness was 0.3 or 0.4 nm. The measured weight gain was 0.20 to 0.32 mg for samples of area of 105−120 mm$^2$. The forest heights range from 6.0 to 9.9 $\mu$m. The mass density derived from this varies from 0.248 to 0.38 ± 0.0046 g/cm$^3$. The resulting area density is in the range of 1.07 to 1.64 × $10^{13}$ cm$^{-2}$ for mean SWNT diameters of 1.0 nm.

We have also used the liquid-induced compaction method to estimate the CNT density. The sample is soaked in ethanol and dried in air to obtain the filling factor.[1] Figure 4a,b compares top view SEM images of a highest density and a standard forest after the compaction process. The tops of the compacted regions are colored red. The filling fraction is 71% for a high-density forest (Figure 4a) and 6.4% for a standard forest (Figure 4b) prepared using 1% $C_2H_2$ and 0.7 nm Fe. A SEM cross section (Figure 4c) shows that nanotubes at the edges are broken at their roots and shift toward the center of SWNT blocks. This image also shows that the density does not vary much with height in the forest.

The filling factor is given by $F = (D + \delta_2)/(D + \delta_1)$, where $\delta_1$ is the average wall-to-wall spacing in the as-grown state and $\delta_2$ is this spacing in the liquid-compacted state. The area density is then given by $N = 2/(3^{1/2}(D + \delta_2)^2)$. The ratio of $F$ = 71% to $F$ = 6.4% suggests a roughly 10-fold increase in $F$ between the dense forests and the standard forests if the compacted density is the same for both cases. (The area density of the standard forests is known to greater accuracy because these are higher, and weight gain is more reliable for them.) The compacted density is estimated to be about 0.9 g/cm$^3$, similar to that found by Futaba[1] and less than the ideal compacted value of 1.5 g/cm$^3$ for a 1.0 nm diameter array[45] because the CNTs are not completely straight and do cross over each other. As $\delta_1 \gg D$, this is roughly consistent with a 10-fold increase in area density found by the weight gain method.

Figure 5 shows some cross-section SEM images of the forests. The nanotubes are seen to be very straight,

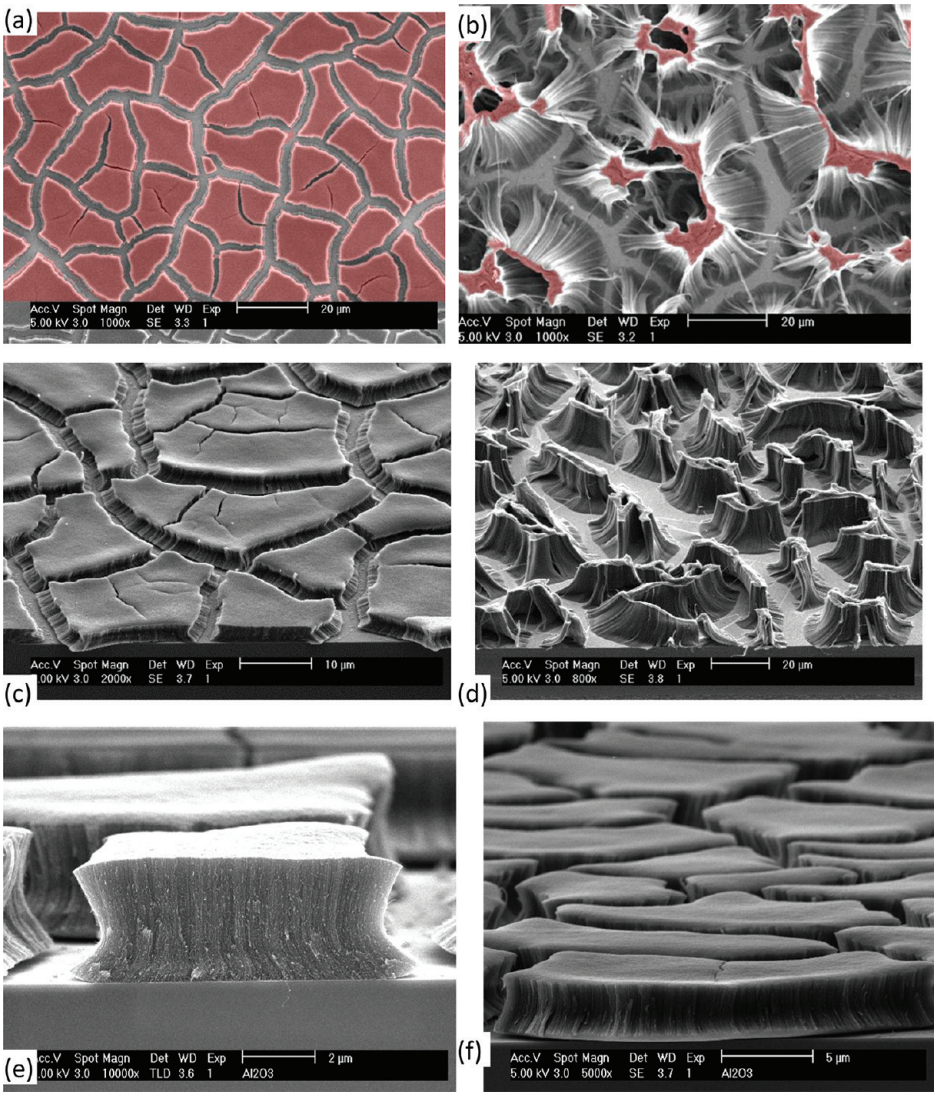


**Figure 4. Liquid-induced densification of different SWNT forests by soaking the samples with ethanol and drying in air. (a) Ultradense SWNT sample shown in Figure 3 grown in 8% $C_2H_2$ and 0.5 nm Al/0.4 nm Fe/5 nm Al/Si(100). (b) Standard SWNT forest grown for 1% $C_2H_2$ on 0.5 nm Al/0.7 nm Fe/5 nm Al/Si(100); other conditions same as (a). Tilted SEM images of liquid compacted (c) ultradense and (d) standard forests of similar heights, showing the clearly higher density of (c). (e) Cross-sectional details of the densification effect, a corner showing that the compaction does not vary much with height, implying that the density is reasonably homogeneous. (f) Wide view of cracking.**

consistent with the high density and the crowding mechanism of alignment. The top of the forest is seen to be the densest, whereas the lower forest (which grows later, in root growth) is seen to be less dense. This is perhaps because some catalyst particles are becoming deactivated. Thus, the area density derived by weight gain is an average value.

A density of $1.48 \times 10^{13}$ cm$^{-2}$ is the highest value so far achieved for a simple catalyst preparation procedure. It is a factor 20 times greater than the previous typical nanotube forests of Futaba,[1] Zhong,[10] or Nessim[31] (see Figure 1). It is also significantly larger than the densities found in the recent work of Yokoyama,[23] Yamazaki,[25] or Dijon[28] on vias. These CNTs had larger average diameters than here. Our density is comparable with the density achieved by the recent cyclic catalyst process of Esconjauegui.[32] Note that the nanotube mats of Yamazaki[25] are actually more space filling than ours, but they have a larger diameter, so that their area density is not as high as here. Our area density is 3 orders of magnitude higher than the typical $10^9$–$10^{10}$ cm$^{-2}$ found for horizontally aligned nanotube arrays grown on quartz or sapphire.[43,44] This is not surprising as these substrates are optimal for horizontal alignment, not for high-density growth. The mass density of our forest of 0.25–0.35 g/cm$^3$ compares with previous values of 0.06 g/cm$^3$,[10] which indicates how much denser the new forests are.

Figure 6a plots the nanotube length taken from SEM side views of forest height *versus* the $C_2H_2$ partial pressure during growth for two different Fe catalyst thicknesses.

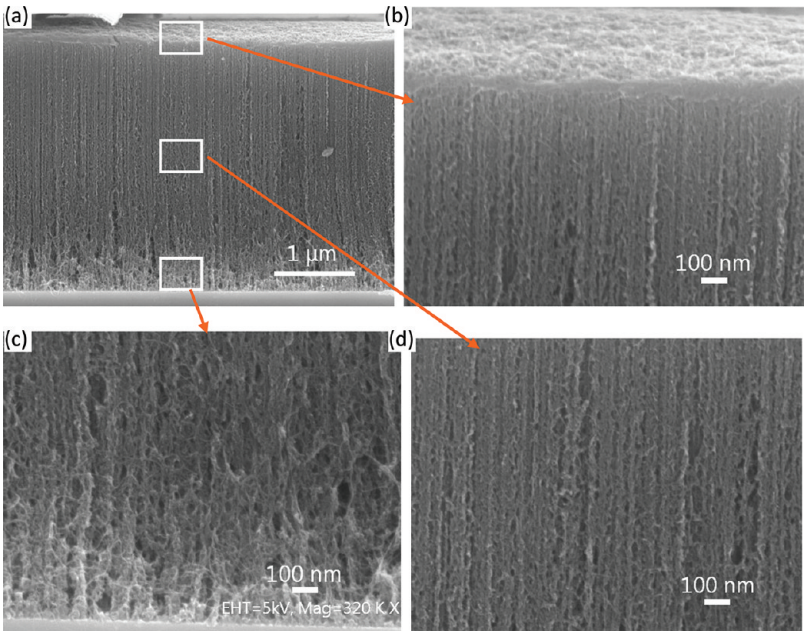


**Figure 5. Cross-sectional SEM images of the ultradense SWNT forests (a), showing close-ups of three zones from top to bottom of the forest (b–d). Grown at 8% $C_2H_2$ 15 mbar total pressure and 700 °C on 0.5 nm Al/0.3 nm Fe/5 nm Al/Si(100).**

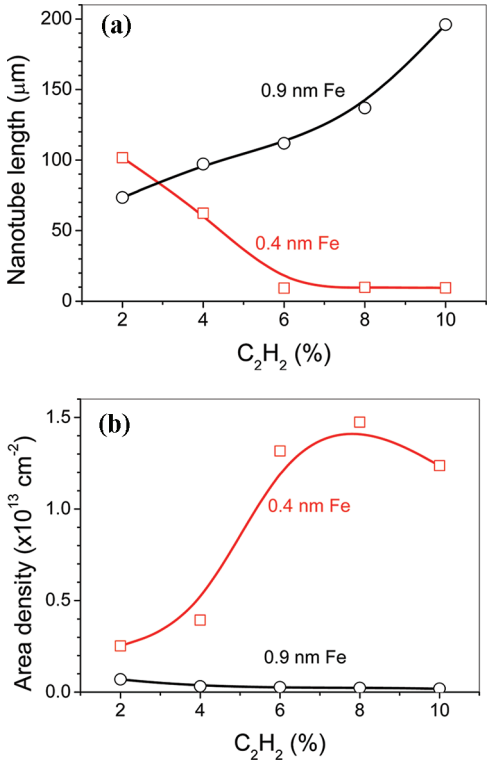


**Figure 6. (a) Nanotube length *vs* $C_2H_2$ fraction in growth gas for 0.4 and 0.9 nm thick Fe catalyst. (b) Area density derived from weight gain for 0.4 and 0.9 nm Fe catalyst *vs* percent $C_2H_2$, at 15 mbar total pressure and 700 °C for 0.5 nm Al/Fe/5 nm Al/Si(100).**

We see that the length increases progressively with $C_2H_2$ partial pressure for the 0.9 nm thick Fe, as expected as the growth rate is proportional to partial pressure to the half power.[46] On the other hand, the growth rate decreases with $C_2H_2$ partial pressure for the 0.4 nm thick Fe case. We tentatively attribute this to diffusion-limited gas access in the denser forests.

Figure 6b shows the area density deduced from weight gain measurements for the two cases. We see that the area density corresponds about $10^{12}$ $cm^{-2}$ for the 0.9 nm Fe case. On the other hand, the area density increases strongly with $C_2H_2$ partial pressure for the thin 0.4 nm case. This shows that there is a changeover in behavior, with the highest density only occurring for the thinner Fe layer and higher $C_2H_2$ partial pressure. The higher density case leads to a lower growth rate. This is not fully understood at present.

Figure 7 shows some SEM images of forests grown from 10 $\mu$m patterned catalyst layers for various Fe thickness and various $C_2H_2$ partial pressures, each for the same growth times. The short forests from the 0.4 nm Fe and 8% $C_2H_2$ grow to the same height in the patterned and unpatterned cases, showing that the diffusion distance would be under 10 $\mu$m.

Finally, we characterized the high-density nanotube forests by resonant Raman spectroscopy. The overall Raman spectrum is shown in Figure 8a at two different places on the forest, for top illumination, grown at 8% $C_2H_2$, showing that the sample is uniform. Figure 8b shows the radial breathing modes (RBMs) measured at different laser excitation wavelengths. The presence of strong RBM modes confirms that the nanotubes are SWNTs, as seen by TEM. The RBMs are excited when a given mode is in resonance with that particular excitation energy. We have assigned the chiral indices of each RBM peak, based on previous assignments for wavenumber and excitation

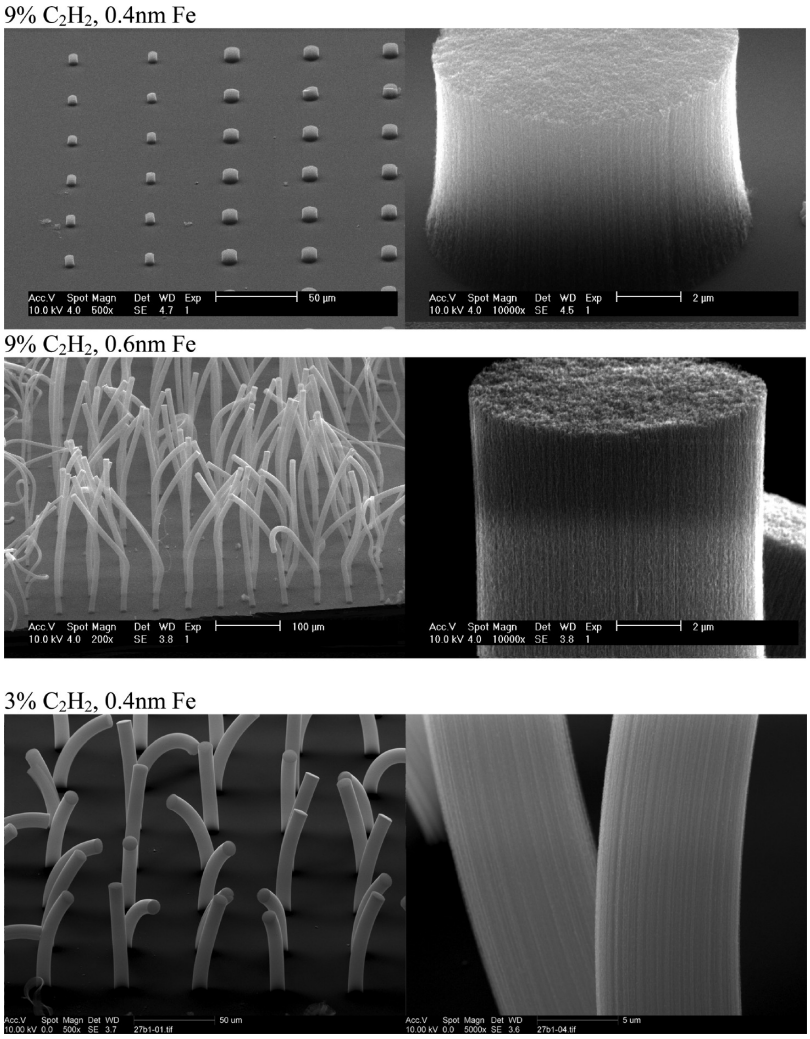


**Figure 7. SEM images of growth from patterned catalysts for various catalyst thickness and % $C_2H_2$ at 15 mbar total pressure and 700 °C for 0.5 nm Al/Fe/5 nm Al/Si(100).**

energy,[47−51] which are based on Kataura plots offset by exciton binding energies. The RBM wavenumber $\omega$ ($cm^{-1}$) is known to depend on the SWNT diameter $D$ (nm) according to the usual formula,[46] $\omega = C_1/D + C_2$, and we find by fitting (Figure 8c) that $C_1 = 212.36$ and $C_2 = 20.07$.

The RBM spectra are consistent with the diameter distribution found by TEM. After subtracting the background, the spectra are relatively flat and featureless below 150 $cm^{-1}$ in Figure 8b, except for one mode at 145 $cm^{-1}$ in the 780 nm spectrum. Converting this into diameters, as in the upper scale on Figure 8b, there are few CNTs with diameters above 1.5 nm. Note that the multiple small peaks in the 100 $cm^{-1}$ range in the 465 and 502 nm spectra are due to molecule excitations in the atmosphere, while the intensity increase at low Raman shift is due to the laser line.

Raman is useful because it detects both metallic and semiconducting nanotubes, in contrast to say photoluminescence excitation. This allows us to derive the fraction of metallic tubes, once we have an estimate for the variation of Raman intensity with chiral angle. Using established intensity relationships,[48,52−54] we find that the forests have a range of chiralities, with some excess of metallic nanotubes over the random 1/3:2/3 distribution. We find 43% metallic and 57% semiconducting tubes. The chirality distribution is biased toward the armchair side, as in other work, but the low chiral angles near armchair are preferred over the armchairs themselves. Figure 8c shows the actual dominant chirality distribution. We note that previous analysis of high-density forests of larger diameter CNTs found a roughly random distribution.[49,51] On the other hand, control of the catalyst or growth conditions can be used to control the chirality distribution to be highly semiconducting or, in a very few cases, mainly metallic.[55−57] Some growth mechanisms give a chiral angle distribution biased toward armchair growth.[58] Clearly, the application to interconnects requires metallic nanotubes.

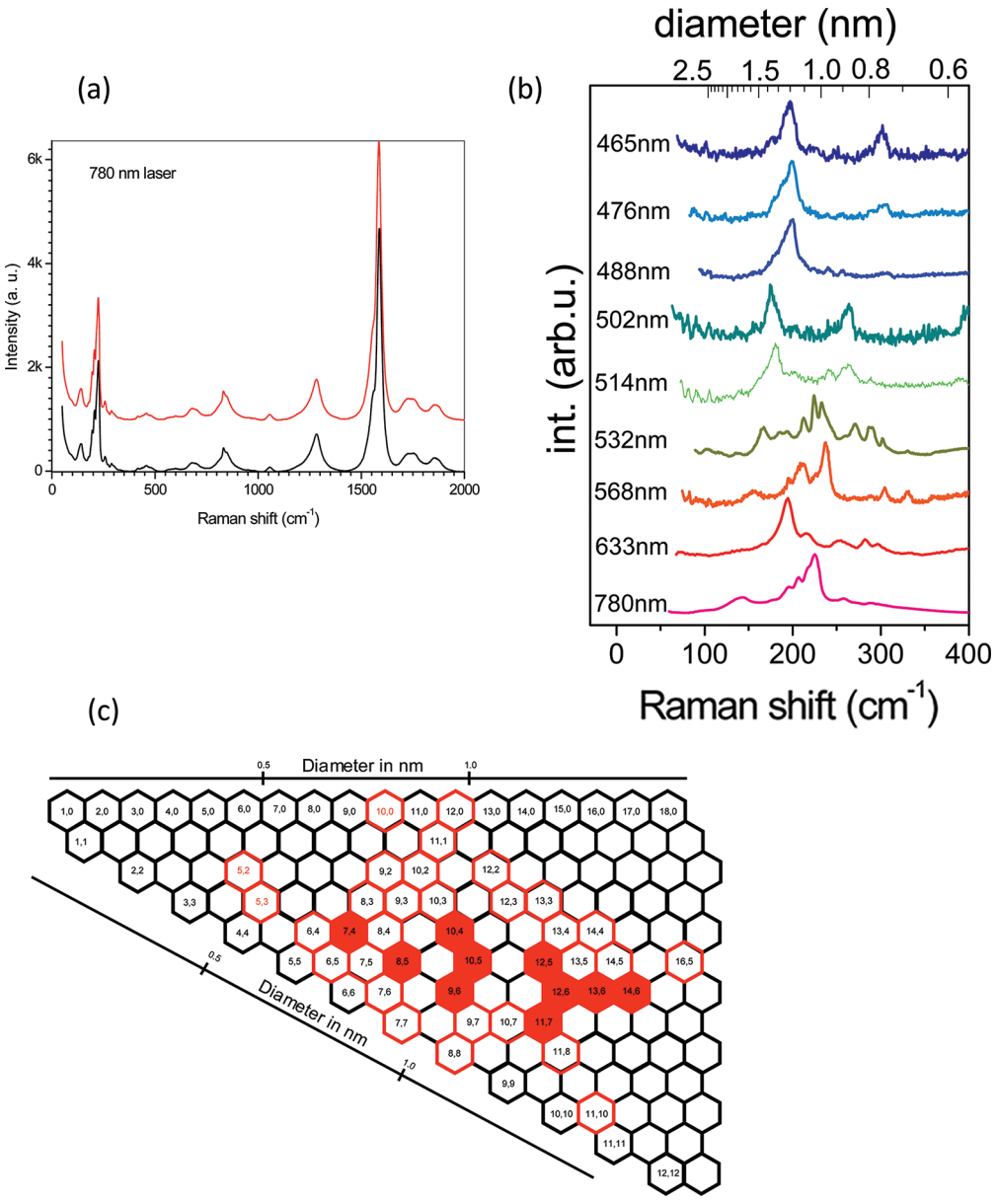


**Figure 8. (a) Raman spectra measured at two different places of a sample of ultrahigh density SWNT forests grown at 8% $C_2H_2$ 15 mbar total pressure and 700 °C on 0.5 nm Al/0.3 nm Fe/5 nm Al/Si(100). Top illumination. The spectra were normalized to the G bands at about 1588 $cm^{-1}$, and the laser excitation wavelength is 780 nm. (b) Radial breathing mode spectra measured at the indicated laser wavelengths. Diameter scale taken from chirality fitting. (c) Chirality distribution based on our (*m*,*n*) assignments.**

## CONCLUSIONS

The average diameter of nanotubes grown by CVD can be reduced toward 1.0 nm if the initial catalyst thickness can be reduced toward 0.3 nm, provided that the growth yield can be maintained by improving the diffusion barrier properties of the catalyst support layer. We have used a 0.5 nm Al/0.3−0.4 nm Fe/5 nm Al nanolaminate catalyst, with the 5 nm Al lower barrier layer pretreated by, for example, an $O_2$ plasma before coating the Fe catalyst. The highly dense SWNT forests are grown by a cold-wall CVD to minimize catalyst sintering. The area density of the as-grown SWNT forests was measured by weight gain and TEM image analysis to be $1.5 \times 10^{13}/cm^2$, the highest presently reached, due to the reduction in the average nanotube diameter.

## METHODS

The $Al_2O_3$ catalyst support was made by depositing 5 nm Al by DC sputtering and subjecting it to an $O_2$ plasma at 0.15 mbar, 20 sccm $O_2$, with 100 W RF power, at room temperature for 20 min. The Fe layer is deposited by sputtering, with the thickness calibrated from the deposition time with growth rate determined elsewhere by XPS, spectroscopic ellipsometry, and

weight gain. The top $Al_2O_3$ layer is deposited as Al by sputtering and is then oxidized by ambient air.

Nanotube growth is carried out in a cold-wall CVD chamber at 700 °C for 3 min at 15 mbar total gas pressure, using $H_2$ diluted $C_2H_2$, with the $C_2H_2$ gas flow ratio varying between 1% and 8%. Prior to the introduction of the $C_2H_2$, the catalyst is exposed to a pure $H_2$ gas flow for 5 min. The sample temperature is ramped up rapidly at 250 °C/min to minimize Ostwald ripening of the catalyst.

The resulting nanotube forests are characterized by scanning electron microscopy (SEM, Philips XL30 SFEG and Zeiss nvision SEM/FIB) and high-resolution transmission electron microscopy (HRTEM, JEOL 4000) operating at 80 keV. The samples for TEM were prepared by rubbing a lacey carbon-coated copper TEM grid on the SWNT forests, which led to the break up of the forest and CNTs from bundle surfaces being transferred to the grid.

SIMS and Auger were carried out by Loughborough Surface Analysis Ltd. as a service. An $^{18}O$ ion beam system was used for the SIMS analysis. The AFM image was collected on a "Dimension" AFM in height mode at 512 Hz.

The nanotube area density is primarily determined by weight gain. The catalyst sample weight is measured before and after growth by a Satorius microbalance (ME235S, 0.01 mg). The samples have total weight of 120−145 mg. Tests of the measurement drift confirmed that this is on the order of 0.003 mg.

The multi-wavelength Raman spectra were measured illuminating the top surface of the forests using a confocal micro-Raman system (Dylor XY800) with triple monochromator in backscattering geometry for laser energies of 2.66−2.41 and 2.18 eV. For 2.33 and 1.96 eV, a Labram (Horiba Jobin Yvon) system is used.

*Conflict of Interest:* The authors declare no competing financial interest.

*Acknowledgment.* We thank C. Thomsen in TU Berlin for use of Raman facilities, H. Liang of Schlumberger Research, Cambridge, for use of the microbalance, and F. Yan for some catalyst preparation. Support by the European Community (VIACARBON) is gratefully acknowledged. J.H.W. thanks support from the Glasstone Fund and Brasenose College, Oxford.

*Supporting Information Available:* Supporting material is available. This material is available free of charge *via* the Internet at http://pubs.acs.org.

## REFERENCES AND NOTES

1. Futaba, D. N.; Hata, K.; Yamada, T.; Hiraoka, T.; Hayamizu, Y.; Kakudate, Y.; Tanaike, O.; Hatori, H.; Yumura, M.; Iiijima, S. Shape-Engineerable and Highly-Dense Packed Single-Walled Carbon Nanotubes and Their Application as Super-capacitor Electrodes. *Nat. Mater.* **2006**, *5*, 987–994.
2. Izadi-Najafabadi, A.; Yasuda, S.; Kobashi, K.; Yamada, T.; Futaba, D. N.; Hatori, H.; Yumura, M.; Iijima, S.; Hata, K. Extracting the Full Potential of Single-Walled Carbon Nanotubes as Durable Supercapacitor Electrodes. *Adv. Mater.* **2010**, *22*, E235–E241.
3. Qu, L.; Dai, L.; Stone, M.; Xia, Z.; Wang, Z. L. Carbon Nanotube Arrays with Strong Shear Binding-on and Easy Normal Lifting-off. *Science* **2008**, *322*, 238–242.
4. Hata, K.; Futaba, D. N.; Mizuno, K.; Namai, T.; Yumura, M.; Iijima, S. Water-Assisted Highly Efficient Synthesis of Impurity-Free Single-Walled Carbon Nanotubes. *Science* **2004**, *306*, 1362–1364.
5. Murakami, Y.; Chiashi, S.; Miyauchi, Y.; Hu, M.; Ogura, M.; Okubo, T.; Maruyama, S. Growth of Vertically Aligned Single-Walled Carbon Nanotube Films on Quartz Substrates. *Chem. Phys. Lett.* **2004**, *385*, 298–303.
6. Zhong, G. F.; Iwasaki, T.; Honda, K.; Furukawa, Y.; Ohdomari, I.; Kawarada, H. Low Temperature Synthesis of Extremely Dense, Vertically Aligned Single-Walled Carbon Nanotubes. *Jpn. J. Appl. Phys.* **2005**, *44*, 1558–1561.
7. Noda, S.; Hasegawa, K.; Sugime, H.; Kakehi, K.; Zhang, Z. Y.; Maruyama, S.; Yamaguchi, Y. Millimeter-Thick Single-Walled Carbon Nanotube Forests: Hidden Role of Catalyst Support. *Jpn. J. App. Phys.* **2007**, *46*, L399–L401.
8. Futaba, D. N.; Hata, K.; Yamada, T.; Mizuno, K.; Yumura, M.; Iijima, S. Kinetics of Water-Assisted Single-Walled Carbon Nanotube Synthesis Revealed by Time-Evolution Analysis. *Phys. Rev. Lett.* **2005**, *95*, 056104.
9. Yamada, T.; Maigne, A.; Yudasaka, M.; Mizuno, K.; Futaba, D. N.; Yumura, M.; Iijima, S.; Hata, K. Revealing the Secret of Water-Assisted Carbon Nanotube Synthesis by Microscopic Observation of the Interaction of Water on the Catalysts. *Nano Lett.* **2008**, *8*, 4288–4292.
10. Zhong, G. F.; Iwasaki, T.; Kawarada, H. Semi-quantitative Study on the Fabrication of Densely-Packed and Vertically Aligned Single-Walled Carbon Nanotubes. *Carbon* **2006**, *44*, 2009–2014.
11. Zhong, G. F.; Iwasaki, T.; Robertson, J.; Kawarada, H. Growth Kinetics of 0.5 cm Vertically-Aligned Single-Walled Carbon Nanotubes. *J. Phys. Chem. B* **2007**, *111*, 1907–1910.
12. Meshot, E. R.; Hart, A. J. Abrupt Self-termination of Vertically Aligned Carbon Nanotube Growth. *Appl. Phys. Lett.* **2008**, *92*, 113107.
13. Vinten, P.; Marshall, P.; Lefebvre, J.; Finnie, P. Distinct Termination Morphologies for Vertically-Aligned Carbon Nanotube Forests. *Nanotechnology* **2010**, *21*, 035603.
14. Amama, P. B.; Pint, C. L.; McJilton, L.; Kim, S. M.; Stach, E. A.; Murray, P. T.; Hauge, R. H.; Maruyama, B. Role of Water in Super Growth of Single-Walled Carbon Nanotube Carpets. *Nano Lett.* **2009**, *9*, 44–49.
15. Kim, S. M.; Pint, C. L.; Amama, P. B.; Hauge, R. H.; Maruyama, B.; Stach, E. A. Catalyst and Catalyst Support Morphology Evolution in Single-Walled Carbon Nanotube Supegrowth. *J. Mater. Res.* **2010**, *25*, 1875–1885.
16. Hasegawa, K.; Noda, S. Millimeter Tall Single wall Carbon Nanotubes Rapidly Grown with and without Water. *ACS Nano* **2011**, *5*, 975–984.
17. Jackson, J. J.; Puretzky, A. A.; More, K. L.; Rouleau, C. M.; Eres, G.; Geohegan, D. B. Pulsed Growth of Vertically Aligned Nanotube Arrays with Variable Density. *ACS Nano* **2010**, *4*, 7573–7581.
18. Xiang, R.; Yang, Z.; Zhang, Q.; Luo, G.; Qiaun, W.; Wei, F.; Kadowaki, M.; Einarsson, E.; Maruyama, S. Growth Deceleration of Vertically Aligned Carbon Nanotube Arrays, Catalyst De-activation or Feedstock Diffusion Control? *J. Phys. Chem. C* **2008**, *112*, 4892–4896.
19. Kreupl, F.; Graham, A. P.; Duesberg, G. S.; Steinhoegl, W.; Liebau, M.; Unger, E.; Honlein, W. Carbon Nanotubes in Interconnect Applications. *Microelectron. Eng.* **2002**, *64*, 339.
20. Robertson, J.; Zhong, G.; Hofmann, S.; Bayer, B. C.; Esconjauregui, C. S.; Telg, H.; Thomsen, H. Use of Carbon Nanotubes for VLSI Interconnects. *Diamond Relat. Mater.* **2008**, *18*, 957–962.
21. Wei, B. Q.; Vajtai, R.; Ajayan, P. M. Reliability and Current Carrying Capacity of Carbon Nanotubes. *Appl. Phys. Lett.* **2001**, *79*, 1172–1174.
22. Nihei, M.; Horibe, M.; Kawabata, A.; Awano, Y. Simultaneous Formation of Multi-wall Carbon Nanotubes and Their End-Bonded Ohmic Contacts to Ti Electrodes for Future ULSI Interconnects. *Jpn. J. Appl. Phys.* **2004**, *43*, 1856–1859.
23. Yokoyama, D.; Iwasaki, T.; Ishimaru, K.; Sato, S.; Hyakushima, T.; Nihei, M.; Awano, Y.; Kawarada, H. Low Temperature Grown Carbon Nanotube Interconnects Using Inner Shells by Chemical Mechanical Polishing. *Appl. Phys. Lett.* **2007**, *91*, 263101.
24. Yamazaki, Y.; Sakuma, N.; Katagiri, M.; Suzuki, M.; Sakai, T.; Sato, S.; Nihei, M.; Awano, Y. High Quality Carbon Nanotube Growth at Low Temperature by Pulsed Remote Plasma Chemical Vapor Deposition. *Appl. Phys. Express* **2008**, *1*, 034004.
25. Yamazaki, Y.; Saluma, N.; Katagiri, M.; Suzuki, M.; Sakai, T.; Sato, S.; Nihei, M.; Awano, Y. Synthesis of a Closely Packed Carbon Nanotube Forest by a Multi-Step Growth Method Using Plasma-Based Chemical Vapor Deposition. *Appl. Phys. Express* **2010**, *3*, 055002.
26. Awano, Y.; Sato, S.; Nihei, M.; Sakai, T.; Ohno, Y.; Mizutani, T. Carbon Nanotubes for VLSI, Interconnect and Transistor Applications. *Proc. IEEE* **2011**, *98*, 2015.

27. Dijon, J.; Fournier, A.; Szkutnik, P. D.; Okuno, H.; Jayet, C.; Fayolle, M. Carbon Nanotubes for Interconnects in Future Integrated Circuits. *Diamond Relat. Mater.* **2010**, *19*, 382–388.
28. Dijon J.; Okuno H.; Fayolle M.; Vo T.; Pontcharra J.; Acquiviva D.; Ionescu A M.; Esconjauregui C S.; Capraro B.; Robertson J. *Ultrahigh Density Carbon Nanotubes on Al-Cu for Advanced Vias*; Electron Devices Meeting, **2010**; p 32.6
29. Close, G. F.; Yasuda, S.; Paul, B.; Fujita, S.; Wong, H. S. P. 1 GHz Integrated Circuit with Carbon Nanotube Interconnects and Silicon Transistors. *Nano Lett.* **2008**, *8*, 706–709.
30. Nessim, G. D.; Seita, M.; O'Brien, K. P.; Hart, A. J.; Bonaparte, R. K.; Mitchell, R. R.; Thompson, C. V. Low Temperature Synthesis of Vertical Aligned Carbon Nanotubes with Electrical Contact to Metallic Substrates Enabled by Thermal Decomposition of Carbon Feedstock. *Nano Lett.* **2009**, *9*, 3398–3405.
31. Esconjauregui, S.; Fouquet, M.; Bayer, B. C.; Ducati, C.; Smajda, R.; Hofmann, S.; Robertson, J. Growth of Ultrahigh Density Vertically Aligned Carbon Nanotube Forests for Interconnects. *ACS Nano* **2010**, *4*, 7431–7436.
32. Kataura, H.; Kumazawa, Y.; Maniwa, Y.; Umezu, I.; Suzuki, S.; Ohtsuka, Y.; Achiba, Y. Optical Properties of Single Wall Carbon Nanotubes. *Synth. Met.* **1999**, *103*, 2555–2558.
33. Dai, H.; Hafner, J. H.; Rinzler, A. G.; Colbert, D. T.; Smalley, R. E. Nanotubes as Nanoprobes in Scanning Probe Microscopy. *Nature* **1996**, *384*, 147–150.
34. Cheung, C. L.; Kurtz, A.; Park, H.; Lieber, C. M. Diameter Controlled Synthesis of Carbon Nanotubes. *J. Phys. Chem. B* **2002**, *106*, 2429–2433.
35. Bachilo, S. M.; Balzano, L.; Herrera, J. E.; Pompeo, F.; Resasco, D. E.; Weisman, R. B. Narrow (*n*,*m*) Distribution of Sinlge Walled Carbon Nanotubes Grown Using a Solid Supported Catalyst. *J. Am. Chem. Soc.* **2003**, *125*, 11186–11187.
36. Lolli, G.; Zhang, L.; Balzano, L.; Sakulchaicharoen, N.; Tan, Y.; Resasco, D E. Tailoring (*n*,*m*) Structure of Single Walled Carbon Nanotubes by Modifying Reaction Conditions. *J. Phys. Chem. B* **2006**, *110*, 2108–2115.
37. Kim, D.; Giermann, A. L.; Thompson, C. V. Solid-State De-wetting of Patterned Thin Films. *Appl. Phys. Lett.* **2009**, *95*, 251903–251905.
38. Hofmann, S.; Sharma, R.; Ducati, C.; Du, G.; Mattevi, C.; Cepek, C.; Cantoro, M.; Pisana, S.; Parvez, A.; Cervantes-Sodi, F.; *et al. In-Situ* Observations of Cataylst Dynamics during Surface Bound Carbon Nanotube Nucleation. *Nano Lett.* **2007**, *7*, 602–608.
39. Kakehi, K.; Noda, S.; Maruyama, S.; Yamaguchi, Y. Growth Valley Dividing Single and Multi-walled Carbon Nanotubes; Combinatorial Study of Nominal Thickness of Co Catalyst. *Jpn. J. Appl. Phys.* **2008**, *47*, 1961–1965.
40. Mattevi, C.; Wirth, C. T.; Hofmann, S.; Blume, R.; Cantoro, M.; Ducati, C.; Cepek, C.; Knop-Gericke, A.; Milne, S.; Castellarin-Cudia, C.; *et al. In-Situ* X-ray Photoelectron Spectroscopy Study of Catalyst−Support Interactions and Growth of Carbon Nanotube Forests. *J. Phys. Chem. C* **2008**, *112*, 12207–12213.
41. Amama, P. B.; Pint, C. L.; Kim, S. M.; McJilton, L.; Eyink, K. G.; Stach, E. A.; Hauge, R. H.; Maruyama, B. Influence of Alumina Type in the Evolution and Activity of Alumina-Supported Fe Catalysts in Single-Walled Carbon Nanotube Carpet Growth. *ACS Nano* **2010**, *4*, 895–904.
42. Zhong, G.; Hofmann, S.; Yan, F.; Telg, H.; Warner, J. H.; Eder, D.; Thomsen, C.; Milne, W. I.; Robertson, J. Acetylene, a Key Precursor for Single-Walled Carbon Nanotube Forests. *J. Phys. Chem. C* **2009**, *113*, 17321–17325.
43. Kang, S. L.; Kocabas, C.; Ozel, T.; Kim, M.; Pimparkar, N.; Alam, M. A.; Rotkin, S. V.; Rogers, J. A. High Performance Electronics Using Dense, Perfectly Aligned Arrays of Single Walled Carbon Nanotubes. *Nat. Mater.* **2007**, *2*, 230–236.
44. Akinwande, D.; Paul, N.; Lin, A.; Nishi, Y.; Wong, H. S. P. Surface Science of Catalyst Dynamics for Aligned Carbon Nanotube Synthesis on Full Scale Wafers. *J. Phys. Chem. C* **2009**, *113*, 8002–8008.
45. Ericson, L. M.; *et al.* Macroscopic Neat Single-Walled Carbon Nanotube Fibers. *Science* **2004**, *305*, 1447–1450.
46. Wirth, C. T.; Zhang, C.; Zhong, G; Hofmann, S.; Robertson, J. Diffusion and Reaction Limited Growth of Carbon Nanotube Forests. *ACS Nano* **2009**, *3*, 3560–3566.
47. Telg, H.; Maultzsch, J.; Reich, S.; Heinrich, F.; Thomsen, C. Chirality Distribution and Transition Energies of Carbon Nanotubes. *Phys. Rev. Lett.* **2004**, *93*, 177401–177404.
48. Maultzsch, J.; Telg, H.; Reich, S.; Thomsen, C. Radial Breathing Mode of Single Walled Carbon Nanotubes, Optical Transition Energies and Chiral Index Assignment. *Phys. Rev. B* **2005**, *72*, 205438.
49. Robertson, J.; Zhong, G.; Telg, H.; Thomsen, C.; Warner, J. H.; Briggs, G. A. D.; Dettlaff-Weglikowska, U.; Roth, S. Growth and Characterization of High-Density Mats of Single-Walled Carbon Nanotubes for Interconnects. *Appl. Phys. Lett.* **2008**, *93*, 163111.
50. Araujo, P. T.; Doorn, S. K.; Kilina, S.; Tretiak, S.; Einarsson, E.; Jorio, A. Third and Fourth Optical Transitions in Semiconducting Carbon Nanotubes. *Phys. Rev. Lett.* **2007**, *98*, 067401.
51. Araujo, P. T.; Miciel, I. O.; Pesce, P. B. C.; Pimento, M. A.; Doorn, S. K.; Jorio, A. Nature of the Constant Factor in Relation between Radial Breathing Mode Frequency and the Tube Diameter for Single Wall Carbon Nanotubes. *Phys. Rev. B* **2008**, *77*, 241403.
52. Popov, V. N.; Henard, L.; Lambin, P. Resonant Raman Intensity of the Radial Breathing Mode of Single-Walled Carbon Nanotubes within a Nonorthogonal Tight-Binding Model. *Nano Lett.* **2004**, *4*, 1795–1799.
53. Luo, Z.; Papadimmitrakopoulos, F.; Doorn, S. K. Electron−Phonon Interaction and Its Influence on Reconstruction of Single-Walled Radial Breathing Mode Spectra. *Appl. Phys. Lett.* **2006**, *88*, 073110.
54. Jorio, A.; Fantini, C.; Pimenta, M. A.; Capaz, R. B.; Samsonidze, G. G.; Dresselhaus, G.; Dresselhaus, M. S.; Jiang, J.; Kobayashi, N.; *et al.* Resonant Raman Spectroscopy (*n*,*m*) Dependent Effects in Small Diameter Single Wall Carbon Nanotubes. *Phys. Rev. B* **2005**, *71*, 075401.
55. Harutyunan, A. R.; Chen, G.; Paronyan, T. M.; Pigos, E. M.; Kuznetsov, O. A.; Hewapararaman, K.; Kim, S. M.; Zakharov, D.; Stach, E. A.; Sumanasekera, G. U. Preferential Growth of Single Walled Carbon Nanotubes with Metallic Conductivity. *Science* **2009**, *326*, 116–120.
56. Chiang, W.; Sankara, R. M. Linking Catalyst Composition to Chirality Distributions of As-Grown Single Walled Carbon Nanotubes. *Nat. Mater.* **2009**, *8*, 882–886.
57. Qu, L.; Du, F.; Dai, L. Preferential Growth of Semiconducting Vertically Aligned Carbon Nanotubes for Direct Use in FETs. *Nano Lett.* **2008**, *8*, 2682–2687.
58. Ding, F.; Harutyunan, A. R.; Yakobson, B. I. Dislocation Theory of Chirality Controlled Nanotube Growth. *Proc. Natl. Acad. Sci. U.S.A.* **2009**, *106*, 2506–2509.